J Mater Sci (2008) 43:5905–5923
DOI 10.1007/s10853-008-2848-y

Combustion synthesis/quasi-isostatic pressing of $TiC_{0.7}$–NiTi cermets: microstructure and transformation characteristics

E. R. Strutt · T. Radetic · E. A. Olevsky · M. A. Meyers

Received: 20 May 2008 / Accepted: 30 June 2008 / Published online: 27 July 2008

Abstract $TiC_{0.7}$–NiTi cermets were produced by combustion synthesis followed by quasi-isostatic consolidation while the reaction products were still hot and ductile. The $TiC_{0.7}$–NiTi cermets were characterized by differential scanning calorimetry, room temperature transmission electron microscopy (TEM), and in-situ TEM (temperature varied during observation). The matrix of the as-synthesized 20NiTi, 40NiTi, and 60NiTi composites contains both R and B19′ martensites at room temperature. No distinct R-phase morphology could be imaged. In the B19′ martensite, [011] Type II twinning, $(11\bar{1})$ Type I twinning and (001) compound twinning modes were observed as the lattice invariant shear (LIS) of the R-B19′ transformation. The [011] Type II twinning is often reported as the LIS of the B2-B19′ transformation, but this is the first experimental confirmation of its predicted presence as a qualified LIS of the R-B19′ transformation. The (001) compound twinning mode is responsible for the fine structure of the martensite with a wavy morphology. Nanoscale structures with a thickness of 5 nm were obtained inside the twins. Twinning was also observed at the interface with carbide particles, which confirms that some stress relaxation of the elastic mismatch occurs. At room temperature, the matrix of the 80NiTi composite had the R-phase structure, which appeared with a needle-like morphology. Thermal cycling resulted in the suppression of the R-phase transformation. This is the opposite of the behavior observed in un-reinforced NiTi alloys.

E. R. Strutt · M. A. Meyers (✉)
Materials Science and Engineering Program, Departments of Mechanical and Aerospace Engineering and Nanoengineering, University of California, San Diego, La Jolla, CA 92093-0411, USA
e-mail: mameyers@ucsd.edu

T. Radetic
National Center for Electron Microscopy, Lawrence Berkeley National Laboratory, University of California, Berkeley, CA 94720, USA

E. A. Olevsky
Department of Mechanical Engineering, San Diego State University, San Diego, CA 92182-1323, USA

Introduction and objectives

Combustion synthesis, also called self-propagating high-temperature synthesis (SHS), is a method to produce compounds through gas-less exothermic reactions. Although the principle has been known for over a hundred years, through the well-known thermite reaction ($Al + Fe_2O_3 \rightarrow Al_2O_3 + Fe$) used to join rails, the large number of applications and varied technologies stems from the pioneering work of Merzhanov, Borovinskaya, Gordopolov, and others [1–3] at the Institute for High-Temperature Synthesis. The subject is reviewed by Munir and Anselmi-Tamburini [4] and by Yi and Moore [5].

The second objective of this research (first objective presented in the companion paper [6]) was to investigate the effect of TiC_x inclusions on the martensitic transformations of NiTi. Near stoichiometric NiTi undergoes a martensitic transformation from a cubic phase (B2) to either a rhombohedral phase (R-phase) or a monoclinic phase (B19′). The introduction of TiC_x into NiTi creates internal stresses that should affect the NiTi transformation path and martensite microstructure. Differential scanning calorimetry, room temperature transmission electron microcopy (TEM), and in-situ TEM with observation of the evolving transformation as temperature was varied in both

heating and cooling were used to observe mechanisms of accommodation.

Experimental techniques

The processing procedure is described in the companion paper [6]. The cermets consisted of a NiTi (normal composition) matrix and $TiC_{0.7}$ spheroidal particles. Four cermets with different NiTi contents have been synthesized: 20%, 40%, 60%, and 80% (on a volume basis).

Energy dispersive X-ray analysis

The chemical composition was first studied by microprobe. However, since the interaction volume of the electron beam was larger than the spacing between the carbide particles, it was not possible to get an accurate measurement of the NiTi matrix chemistry by this technique. Consequently, energy dispersive X-ray analysis (EDX) was performed within the transmission electron microscope to determine the chemical composition of the matrix. A Kevex high angle detector (HAD) and a Kevex ultra thin window (UTW) detector were used. A NiTi sample (SE-508) from Nitinol Devices and Components Inc. was used for calibration. Table 1 lists the composition of the NiTi standard as determined by the manufacturer using a Direct Current Plasma Spectrometer. The uncertainty is within 1%.

The NiTi sample from Nitinol Devices and Components was stated by the manufacturer to have a composition of 55.7 wt.% Ni, which corresponds to 50.6 at% Ni. The composition of this NiTi sample was checked by EDX in the TEM using the HAD detector. The composition was determined using both the *k*-factors supplied by the Emispec analytical software and those determined by the National Center for Electron Microscopy. Both sets of *k*-factors provided compositions that matched the manufacturer's reported composition within the 1% experimental uncertainty. Since the match with the manufacturer's reported composition was somewhat closer for the *k*-factors provided by Emispec, those values ($K_{Ni} = 1.489$, $K_{Ti} = 1.213$ for the HAD detector) were used for the analysis of the NiTi matrix of the composites. The NiTi sample was not evaluated in the UTW detector, so all data from the UTW detector were multiplied by normalization factors. These normalization factors were determined by comparing the EDX data from the UTW and HAD detectors taken from the same area of the same sample.

Table 1 Chemical composition of NiTi standard used to determine matrix chemistry of TiC–NiTi composites

Element	Weight percent
Ni	55.7
Ti	Balance
O	0.02
H	<0.0003
Co	0.0273
Fe	0.1800
Cu	<0.0050
C	0.0043

Reporting level ±1%

Transmission electron microscopy

Transmission electron microscopy (TEM) was performed at the National Center for Electron Microscopy on a JEOL 200CX microscope. The TEM foils were prepared by electrodischarge machining the 3 mm diameter samples used for the DSC measurements into disks with 1 mm thickness. These were ground down to 100 μm on a Buehler Minimet polisher, dimpled to <20 μm, and then ion-milled to electron transparency at liquid nitrogen temperature. It is important to note that during the foil preparation, wax was used to attach the samples to the necessary fixtures. This required heating the samples to 180 °C, which was above the A_f temperature. Consequently, the samples were thermally cycled through the transformation during sample preparation. However, since the samples were held at liquid nitrogen temperature during the entire ion-milling process, the martensitic microstructure in the thin foils was formed in the bulk condition.

The NiTi morphology formed in the bulk condition was studied by performing TEM at room temperature. Selected area diffraction patterns, bright field, and dark field images were acquired to determine the presence of the B2, B19′, and R phases and to characterize their morphologies both near and far from the carbide particles. In-situ heating and cooling was used to transform the sample in the transmission electron microscope. The sample holder used was a Gatan 636 double tilt analytical holder with a temperature range between −170 and +150 °C. The samples were heated in stages to 110 °C (above the A_f temperature) and then cooled in stages back to room temperature. Liquid nitrogen was added to cool below room temperature. In-situ heating and cooling was used to investigate the transformation path, martensite nucleation and growth, and the effect of carbide particles on the transformation. The in-situ experiments were performed in stages to record selected area diffraction patterns, bright field and dark field images. The experiments were also recorded on video. The in-situ experiments were performed with the zone axis along the $[\bar{1}\bar{1}1]_{B2}$, so that matrix phase transformations could be easily detected from the selected area diffraction pattern.

To aid identification of the different NiTi phases observed in the electron microscope, diffraction simulations were performed using the software *Desktop Microscopist*

(*Macintosh*). The parameters for the R-phase are from Goo and Sinclair [7] and Hara et al. [8]. The parameters for the B19′ phase are from Hehemann and Sandrock [9]. The lattice parameters, angles, and atom positions used in the simulations are shown in Tables 2–4. The orientation relationships between the parent and martensite phases were also included in the simulations [7, 10]. The simulated selected area diffraction patterns for the B2, R, and B19′ phases were viewed along the $[\bar{1}\bar{1}1]_{B2}$.

Differential scanning calorimetry

Differential scanning calorimetry (DSC) was used to determine the temperatures at which the B2 → B19′ and B2 → *R*→ B19′ transformations in the NiTi occur. The following temperatures were investigated:

R_s	R-phase start temperature
R_f	R-phase finish temperature
M_s	B19′ martensitic start temperature
M_f	B19′ martensitic finish temperature
A_s	reverse transformation start temperature
A_f	reverse transformation finish temperature

The onset temperature (or "start" temperature) for the transformation is defined as the temperature at which the heat flow first deviates from the baseline upon cooling. This is because both the formation of the R-phase and the B19′ phase generate heat that can be detected as an exothermic peak on the DSC curve. When no more martensite is formed upon further cooling, the DSC curve returns to the baseline. This point is defined as the finish temperature. It is important to note that start and finish temperatures for these phase transformations are not the same, because the elastic strain energy around the martensite resists further growth unless an additional chemical driving force (i.e., cooling) is available. Upon heating, the reverse transformations appear as endothermic peaks on the DSC curve.

The transformation temperatures were measured with a TA Instruments 2920 DSC. Cylindrical samples, 3 mm in diameter and 4 mm in height, were cut by electro-discharge machining from the 7.5 cm diameter composites. The samples were held at 150 °C for 10 min and then cooled at 5 °C/min to −50 °C. After equilibrating at −50 °C for 10 min, the samples were then heated back to

Table 2 The parameters used for simulation of the B2 NiTi diffraction patterns

Lattice parameters: $\mathbf{a} = \mathbf{b} = \mathbf{c} = 2.998$ Å
Angles: $\alpha = \beta = \gamma = 90°$
Space group: 221 *Pm3m*
Atom positions:

Atom #	*x*	*y*	*z*	Element
1	0	0	0	Ti
2	1/2	1/2	1/2	Ni

Table 3 The parameters used for simulation of the R-phase diffraction patterns

Lattice parameters: $\mathbf{a} = \mathbf{b} = 7.358$ Å, $\mathbf{c} = 5.286$ Å
Angles: $\alpha = \beta = 90°$, $\gamma = 120°$
Space group: 143 *P3*
Atom positions:

wck	*x*	*y*	*z*	Element
a1	0	0	0	Ti
b1	1/3	2/3	0.083	Ti
c1	2/3	1/3	0.009	Ti
d3	0.335	−0.005	0.361	Ti
d3	0.677	0.010	0.684	Ti
a1	0	0	0.457	Ni
b1	1/3	2/3	0.541	Ni
c1	2/3	1/3	0.396	Ni
d3	0.318	−0.022	0.854	Ni
d3	0.688	0.210	0.160	Ni

R-phase orientation relation with parent B2:

Parallel	B2	R-phase	Rotation
Plane	$(\bar{1}11)$	(0001)	0
Direction	[211]	$[2\bar{1}\bar{1}0]$	0

The lattice parameters and orientation relationship are from Goo and Sinclair [7]. The space group is from Hara et al. [8]

Table 4 The parameters used for simulation of the B19′ NiTi diffraction patterns

Lattice parameters: $\mathbf{a} = 2.883$ Å, $\mathbf{b} = 4.117$ Å, $\mathbf{c} = 4.623$ Å
Angles: $\alpha = 90°$, $\beta = 96.8°$, $\gamma = 90°$
Monoclinic
Atom positions:

Atom #	*x*	*y*	*z*	Element
1	0	0	0	Ti
2	0	1/2	0.625	Ti
3	1/2	0	1/2	Ni
4	1/2	1/2	0.125	Ni

B19′ orientation relation with parent B2:

Parallel	B2	B19′	Rotation
Plane	(101)	(001)	−6.5°
Direction	$[\bar{1}11]$	$[\bar{1}10]$	0

The lattice parameters and atom positions are from Hehemann and Sandrock [9]. The orientation relationship between the B19′ and B2 is from Otsuka et al. [10]

150 °C at 5 °C/min. The start and finish temperatures were determined from the intersection of the tangent to curve at the point of maximum slope with the baseline.

To study the effect of thermal cycling on the transformation temperatures and the microstructure, samples were thermally cycled 30 times. This was accomplished by manually transferring them between an oil bath heated to +150 °C and a liquid nitrogen/methanol bath held at −50 °C.

Results and discussion

Chemistry of matrix

Detailed chemical analysis of the matrix of the $TiC_{0.7}$–NiTi samples was performed by EDX in the TEM. Figure 1a shows a NiTi region bounded by two TiC particles for the $TiC_{0.7}$–20NiTi. In Fig. 1c, the profile starts in a TiC_x particle, continues through the NiTi matrix, and then passes

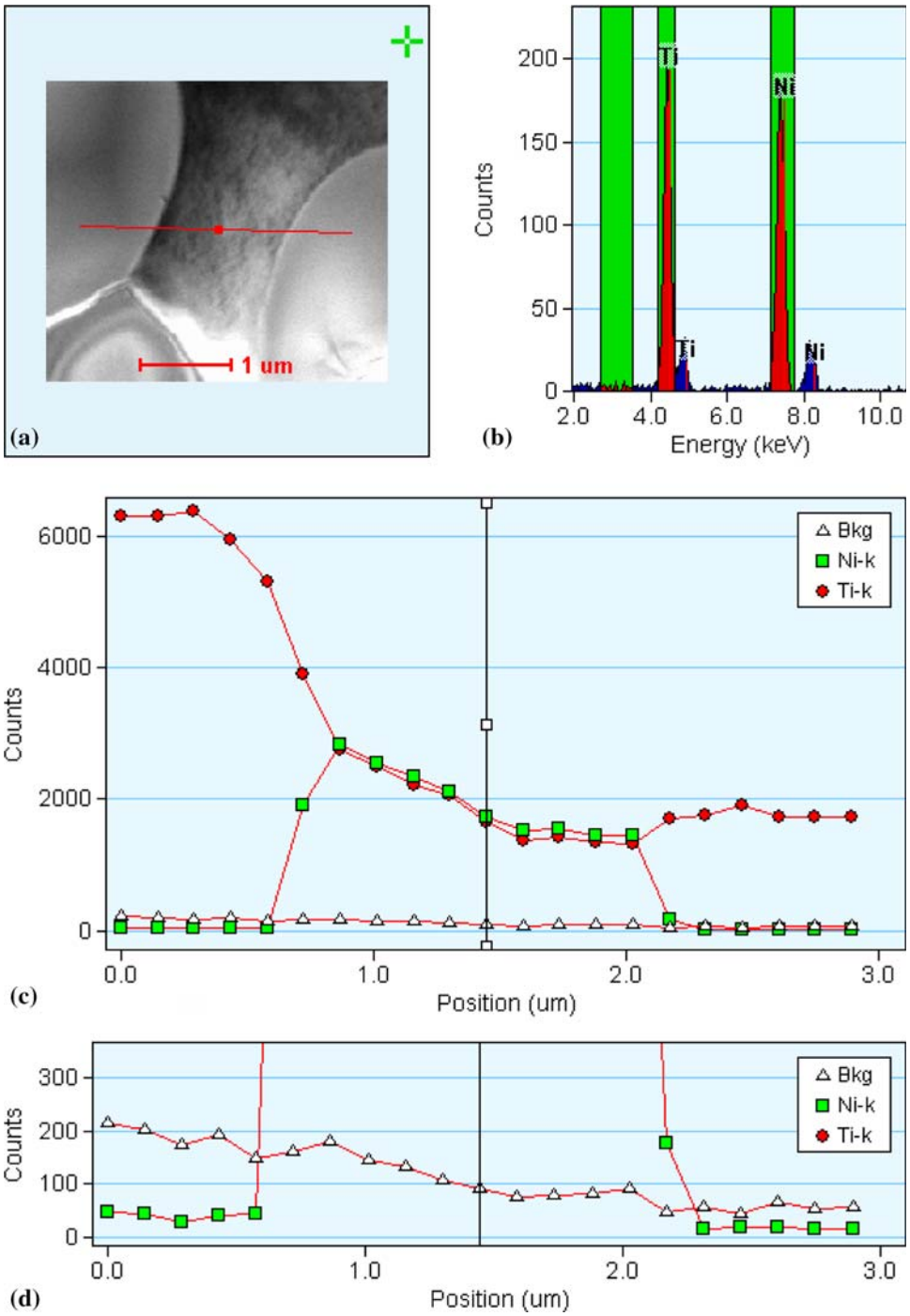

Fig. 1 Concentration profile for the $TiC_{0.7}$–20NiTi measured by EDX in the transmission electron microscope. (**a**) NiTi bounded by TiC_x particles; (**c**) Ni and Ti concentration particles; (**d**) background particles

Table 5 Composition of matrix of 7.6 cm diameter $TiC_{0.7}$–NiTi composites

	Ti atomic percent	Ni atomic percent
20NiTi sample	51.5 (±0.7)	48.5 (±0.7)
40NiTi sample	51.2 (±1.0)	48.8 (±1.0)
60NiTi sample	48.8 (±0.6)	51.2 (±0.6)
80NiTi sample (data acquired in spot mode)	49.7 (±0.6)	50.3 (±0.6)
80NiTi aged (data acquired in spot mode)	44.9 (±1.5)	55.1 (±1.5)

The corresponding standard deviations are presented in parentheses

through another TiC_x particle. In the NiTi matrix, both the Ni and Ti intensities decrease uniformly with one another and with the background spectrum (seen more clearly in Fig. 1d). This reveals that the apparent decline in the Ni and Ti intensities is the result of differences in the thickness of the specimen. The sample gets thinner along the measured profile line, so the overall number of counts measured decreases. The composition of the matrix varies along the profile line between $Ni_{47.6}Ti_{52.4}$ and $Ni_{49.0}Ti_{51.0}$. These differences in apparent composition may be real or they may be due to the preferential absorption of the lower energy X-rays from Ti-$K\alpha$. The average composition, acquired by rastering over several areas of the matrix, is $Ni_{48.5}Ti_{51.5}$. Similarly, the other compositions were also characterized. The average compositions are $Ni_{48.8}Ti_{51.2}$ for $TiC_{0.7}$–40NiTi, and $Ni_{51.2}Ti_{48.8}$ for $TiC_{0.7}$–60NiTi.

The compositions of the as-synthesized and aged $TiC_{0.7}$–80NiTi samples were measured by using the spot mode in the TEM. Each of the values reported in Table 5 is the average of three spot measurements. From these limited number of measurements, the matrix of the aged $TiC_{0.7}$–80NiTi sample appears to have a much higher nickel content than the as synthesized sample. It will be seen later that this has a significant effect on R_s.

Transmission electron microscopy

$TiC_{0.7}$–20NiTi

Figure 2 shows a transmission electron micrograph of the $TiC_{0.7}$–20NiTi composite taken at room temperature. Since the sample was thinned to electron transparency at liquid nitrogen temperature and not subsequently heated above A_s, the structure of the NiTi matrix in Fig. 2 has formed in the bulk condition. This is important, because NiTi is sensitive to the state of stress [11]. When martensite forms in the bulk condition, the surrounding material resists the large strain associated with the change of shape. To reduce the strain, different martensite variants form a self-accommodating structure [12]. This self-accommodating structure is expected to be different if the martensite is formed in the thin foil condition, because it is subject to stress relaxation at the foil surfaces.

In Fig. 2a, the matrix contains regions of light contrast (labeled A) and regions of dark contrast (labeled B). The light regions are located in the broad central portions of the matrix, while the dark areas are located in the narrow corridors between the carbide particles. Figure 2b shows a selected area diffraction pattern taken from region A of Fig. 2a. Reflections appear at the $1/3\{110\}_{B2}$ positions in the $\langle 110\rangle^*_{B2}$reciprocal lattice direction. Comparison of the present results with Fig. 2 of Hwang et al. [13] shows that this pattern is consistent with that of R-phase NiTi.

Figure 3 shows the morphology of the NiTi matrix in region B of Fig. 2a. In the left-hand region (labeled A), there is a large martensite variant that consists of a banded structure. Figure 4 shows the selected area diffraction pattern, which has been rotated to correct for the lens rotation in the microscope. This diffraction pattern is consistent with [011] Type II twinning in B19′ martensite reported first by Knowles and Smith [14] and then confirmed by several researchers [15–17].

In the geometry of the parameters that are used to describe twins, K_1 is the twin plane. It is located at the interface between the two twinned crystals and is a common lattice plane in both structures. During the twinning process, the distances and angles in K_1 are not changed. K_1 also contains the twinning shear direction η_1. K_2 (K_2 before twinning and K_2' after twinning) is the other undistorted plane. η_2 (η_2 before twinning and η_2' after twinning) is the only direction in K_2 that makes the same angle with K_1 both before and after twinning.

The elements for [011] Type II twinning in B19′ NiTi were determined by Knowles and Smith [14] to be: $K_1 = (0.72054\ 1\ \bar{1})$; $\eta_1 = [011]$; $K_2 = (011)$; $\eta_2 = [1\ 0.63583\ -0.63583]$; $s = 0.28040$. It can be seen that η_1 and K_2 have rational indices, while K_1 and η_2 have irrational indices.

In Type II twinning, the two regions are related by a 180° rotation about the twinning shear direction η_1. The spots in the diffraction pattern in Fig. 4 can be indexed consistently if the two regions are related by a 180° rotation about the $[011]_{B19'}$. The zone axis for one pattern (labeled M) appears

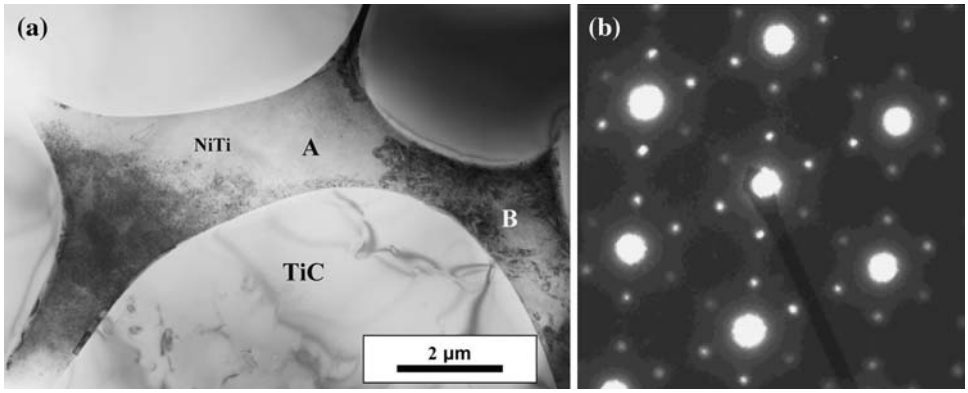

Fig. 2 (**a**) Bright-field image of $TiC_{0.7}$–20NiTi, showing NiTi surrounded by TiC_x particles. (**b**) SAD pattern of Region A in (**a**)

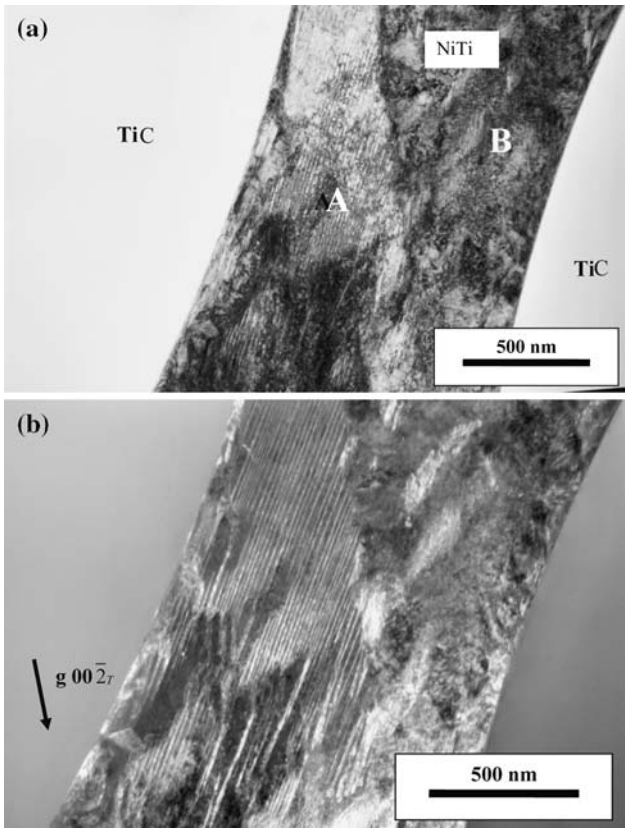

Fig. 3 (**a**) Bright-field of NiTi matrix in Region B of Fig. 2a. (**b**) Dark-field image of lamellar B19′ in matrix of $TiC_{0.7}$–20NiTi

to be along the $[\bar{1}0\bar{1}]_{B19'}$ and the zone axis for the twin pattern (labeled T) appears to be along the $[1\bar{1}0]_{B19'}$. Using the 180° rotation relation, Knowles and Smith [14] calculated that the angular differences between $[\bar{1}0\bar{1}]_M$ and $[1\bar{1}0]_T$ is only 1.8°. Figure 4 shows the indexed pattern, where the common reflection is $(11\bar{1})$.

Figure 3b shows a dark field image of region A in Fig. 3a that was taken with the operative reflection $(00\bar{2})_T$. Since a "twin spot" was used to create the image, the bands oriented with the $[1\bar{1}0_T]$ parallel to the electron beam direction appear with light contrast.

In $TiC_{0.7}$–20NiTi, the [011] Type II twins were observed as the LIS of the R-B19′ transformation, not the B2-B19′ transformation. Mandangopal and Singh [18] have shown that [011] Type II twinning satisfies the phenomenological theory of martensitic transformations for the R-B19′ transformation when the rhombohedral angle reaches the critical value of 86.2°. The observed twin width ratio in $TiC_{0.7}$–20NiTi of 3:1 agrees well with the theoretical value of 2.69:1.

$TiC_{0.7}$–40NiTi

TEM revealed that the matrix of the $TiC_{0.7}$–40NiTi was predominantly B19′ NiTi with some islands of R-phase located in the center of the broad corridors. Figure 5 shows a selected area diffraction pattern of a region of the matrix containing only B19′. Figure 6 shows a dark-field image formed by placing the aperture around one cluster of diffraction spots near the $1/2\{110\}_{B2}$. Three distinct B19′ martensite morphologies can be identified. Adjacent to the TiC_x interface, in Region A, the martensite has a wavy character and each of the bands has an irregular thickness. In Region B, the martensite is lamellar or plate-like. The bands are narrow, straight and have a relatively uniform thickness. In Region C, the variants are somewhat smaller than those in Regions A and B and appear to form a triangular arrangement.

Wavy martensite

Region A in Fig. 6 shows dark field images of wavy B19′ martensite. The top image in Fig. 7 was formed from the $(001)_{M2,T2}$ reflection (marked by a single arrow in Fig. 9). The thickness of the bands varied across their length. For example, measurements of the apparent thickness of a single M2,T2 band (light-band) varied between 10 and 30 nm. The average thickness of several M2,T2 bands, measured across a perpendicular line, was 16 nm.

The bands that appear dark in the top image of Fig. 7, appear light in an image formed with the aperture around

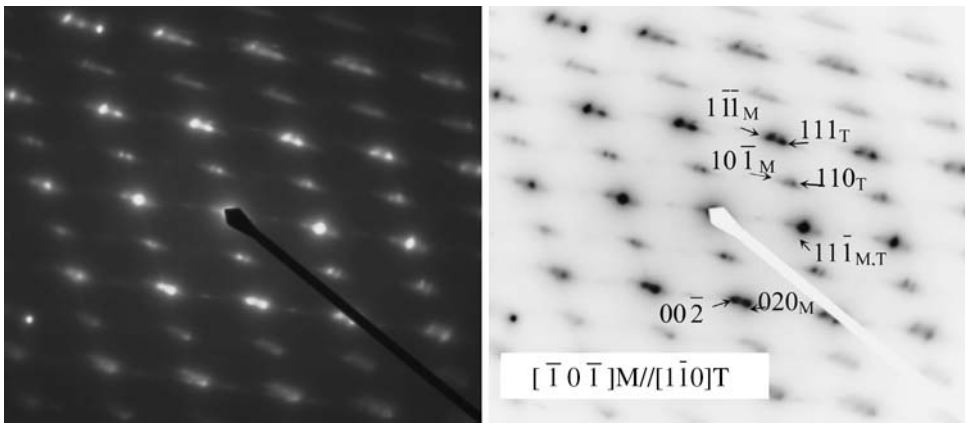

Fig. 4 SAD of lamellar B19′ with [011] Type II twinning

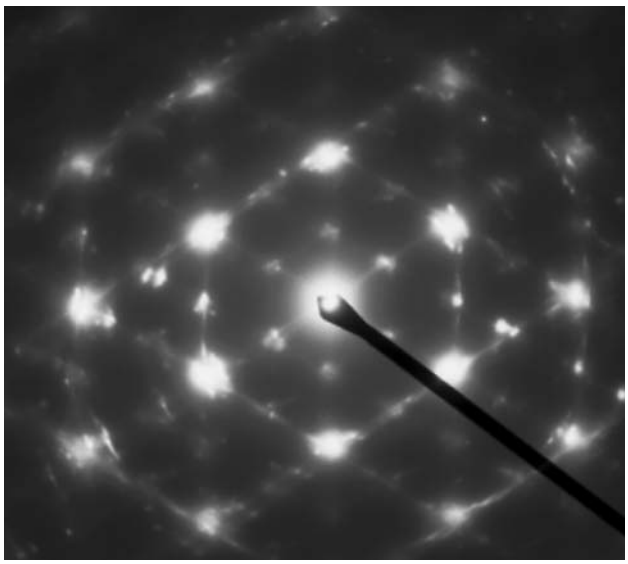

Fig. 5 SAD pattern of matrix of $TiC_{0.7}$–40NiTi composite

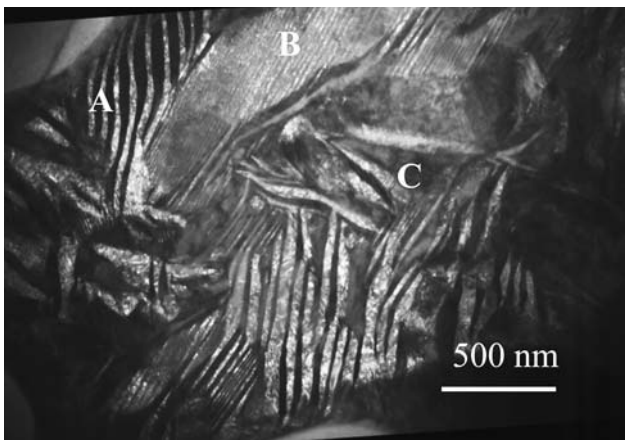

Fig. 6 Dark-field image from one cluster of $1/2\{110\}_{B2}$ reflections in $TiC_{0.7}$–40NiTi

the $(00\bar{1})_{M1,T1}$ reflection (marked by a double arrow in the SAD). The lower picture of Fig. 7 shows this image. The thickness of a single M1,T1 band varied between 14 and

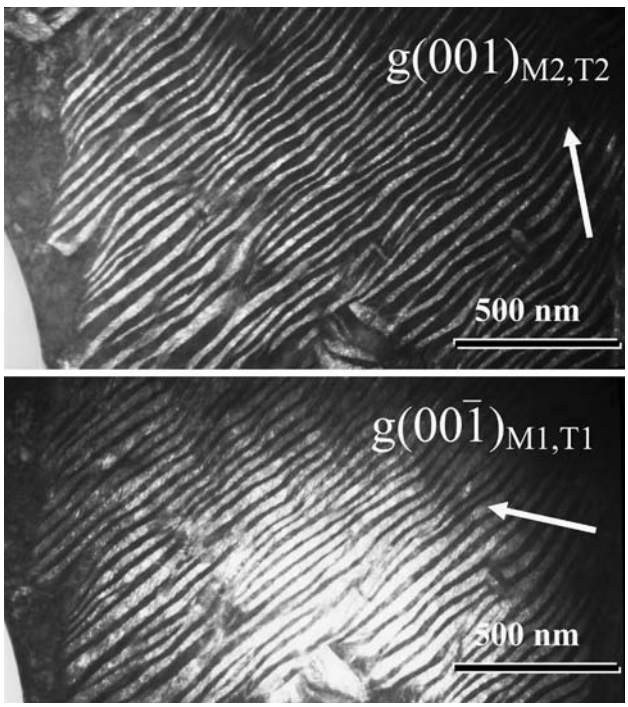

Fig. 7 Wavy martensite in $TiC_{0.7}$–40NiTi

50 nm. The average thickness of many M1,T1 bands was 24 nm.

Wavy martensite has previously been reported in thin foils that have been thermally cycled or held at ambient temperature for several weeks [19]. Wavy martensite has only been reported in samples which also showed the $1/3\{110\}_{B2}$ reflections in the $\langle 111\rangle_{B2}$ diffraction pattern [19]. This is consistent with the current work in which the B2-R-B19′ transformation was observed.

Figure 8 shows that each of the bands of wavy martensite contains an even finer substructure. These nanoscale structures have a thickness of ~5 nm. Selected area diffraction of these wavy bands gives the pattern of reflections shown in Fig. 9. The pattern is similar to Fig. 2b in the work of Madangopal and Singh [18] in which observations

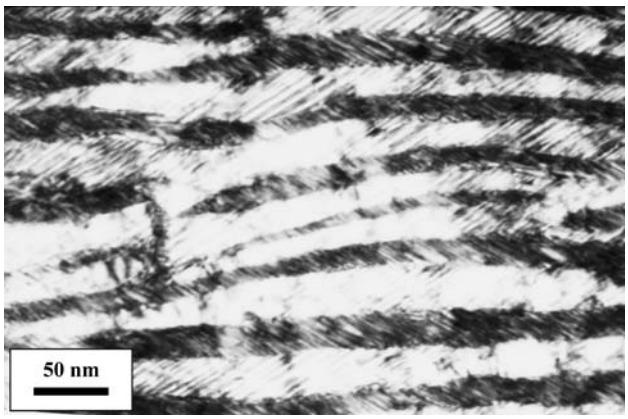

Fig. 8 Internal structure of wavy bands in $TiC_{0.7}$–40NiTi with nanoscale bands

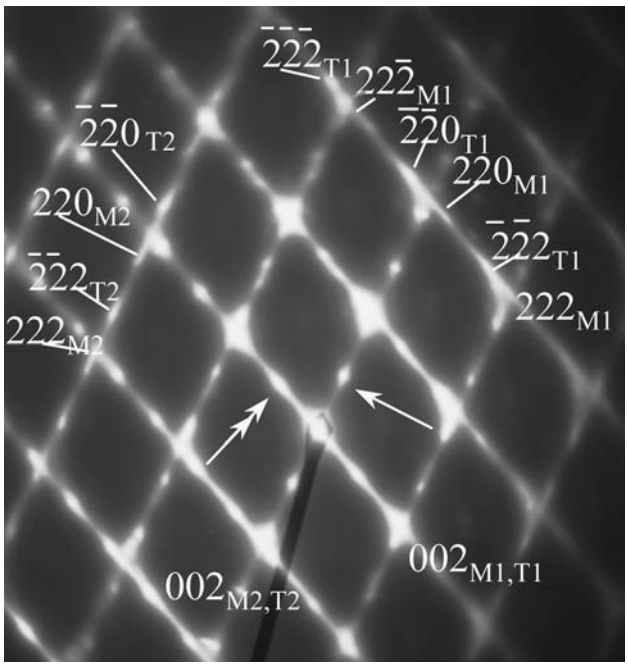

Fig. 9 SAD pattern of wavy B19′ martensite with (001) compound twinning. Beam direction $[\bar{1}10]_{M1}//[1\bar{1}0]_{T1}//[1\bar{1}0]_{M2}//[\bar{1}10]_{T2}$

of wavy martensite were also noted. By taking SAD from within one wavy band, they determined that the substructure of wavy martensite consists of B19′ correspondence variants related by (001)B19′ compound twinning. In Fig. 9 of the present work, taken from many wavy bands, there are four separate patterns of reflections. The patterns labeled M_1 and T_1 are related by mirror symmetry with respect to the $(001)_{M1,T1}$ plane. The patterns labeled M_2 and T_2 are related by mirror symmetry with respect to the $(001)_{M2,T2}$ plane. The overall pattern corresponds to two sets of (001)B19′ compound twins.

The twinning elements for $(001)_{B19'}$ compound twinning, as determined Onda et al. [15], are $K_1 = (001)$, $\eta_1 = [100]$, $K_2 = (100)$, $\eta_1 = [001]$, and $s = 0.23848$. All indices of the twinning elements are rational. The two twin crystals are related by both mirror symmetry with respect to the K_1 plane and by 180° rotation around η_1.

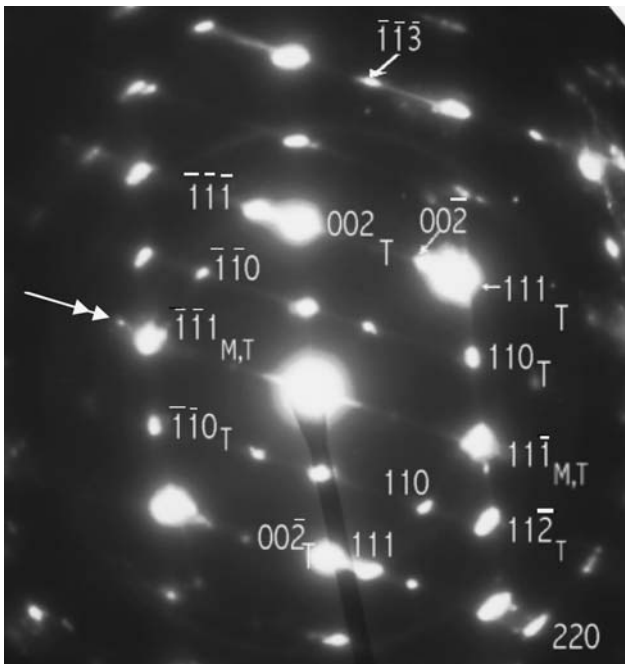

Fig. 10 SAD pattern of lamellar B19′ with $(11\bar{1})$ Type I twinning. Beam direction $[\bar{1}10]_M//[1\bar{1}0]_T$

In Figs. 7–9, the beam direction was $[\bar{1}10]_{M1}//[1\bar{1}0]_{T1}//[1\bar{1}0]_{M2}//[\bar{1}10]_{T2}$, which was perpendicular to the normal to $(001)_{B19'}$. The $(001)_{B19'}$ twins were viewed edge on. It is apparent that the twin thickness (on the order of 1 nm) is much finer than in the [011] Type II twinning mode.

Madangopal and Singh [18] showed that (001) compound twinning does satisfy the phenomenological theory of martensitic transformations for the R-B19′ transformation when the rhombohedral angle reaches the critical angle of 86.2°.

Lamellar martensite

Figure 10 shows the electron diffraction pattern obtained from a region containing lamellar martensite. The pattern, indexed in accordance with Fig. 7b of Xie et al. [17], consists of two sets of reflections that are related to each other by mirror symmetry with respect to the $(11\bar{1})_{M,T}$ plane. This establishes that the alternating platelets are $(11\bar{1})$ Type I twins.

The elements for $(11\bar{1})$ Type I twinning in B19′ NiTi were determined by Knowles and Smith [14] to be: $K_1 = (11\bar{1})$; $\eta_1 = [0.54043\ 0.45957\ 1]$; $K_2 = ((0.24694\ 0.50611\ 1)$; $\eta_2 = [21\bar{1}]]$; $s = 0.30961$. K_1 and η_2 have rational indices. K_2 and η_1 have irrational indices.

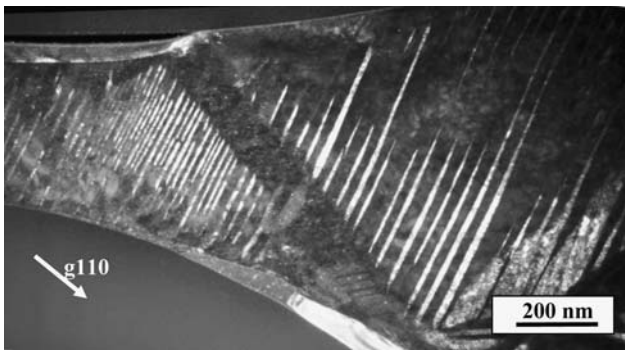

Fig. 11 Lamellar B19′ with $(11\bar{1})$ Type I twinning

Figure 11 shows dark-field images formed by placing the aperture around the $(110)_M$ and $(002)_T$. The beam direction was $[\bar{1}10]_M//[1\bar{1}0]_T$, which was perpendicular to the normal to $(11\bar{1})_{M,T}$. The $(11\bar{1})_{M,T}$ twins were divided into two regions by a 'cross' variant. The twin width on the left side was noticeably smaller than on the right side. On the left, the average thickness of the M bands, which appear bright in Fig. 11, was 6 nm. The average thickness of the T bands, which appear dark in Fig. 11, was 10 nm. The twin width ratio was 1.7:1. On the right, the average thickness of the M bands was 9 nm, the average thickness of the T bands was 33 nm, and the twin width ratio was 3.8:1.

In $TiC_{0.7}$–40NiTi, the $(11\bar{1})$ Type 1 twins were observed as the LIS of the R-B19′ transformation. The phenomenological theory for this twinning mode in the R-B19′ transformation has not yet been carried out.

Localized twinning

Figure 12a shows the B19′ martensite near the carbide interface. Striations appear within the $(11\bar{1})$ twins. Close examination of the SAD pattern in Fig. 10 shows a small spot located near the double arrow. Fig. 12b shows a dark field image taken with the small reflection near the $(11\bar{1})_{M.T}$ spot. This image confirms that the striations are localized to the region near the carbide interface and do not extend throughout the B19′ variant. This localized twinning at the interface between the matrix and reinforcement may be due to relaxation of the elastic mismatch that results during sample processing [20].

$TiC_{0.7}$–60NiTi

Figure 13 shows a global view of the area investigated in the 60NiTi sample. Region A was located near a hole in the foil that was probably formed during the TEM sample preparation. The matrix was composed of many variants of B19′ martensite, most of which had a lamellar morphology as presented for the $TiC_{0.7}$–40NiTi. The diffraction pattern for this region, shown in Fig. 14a, was equivalent to the

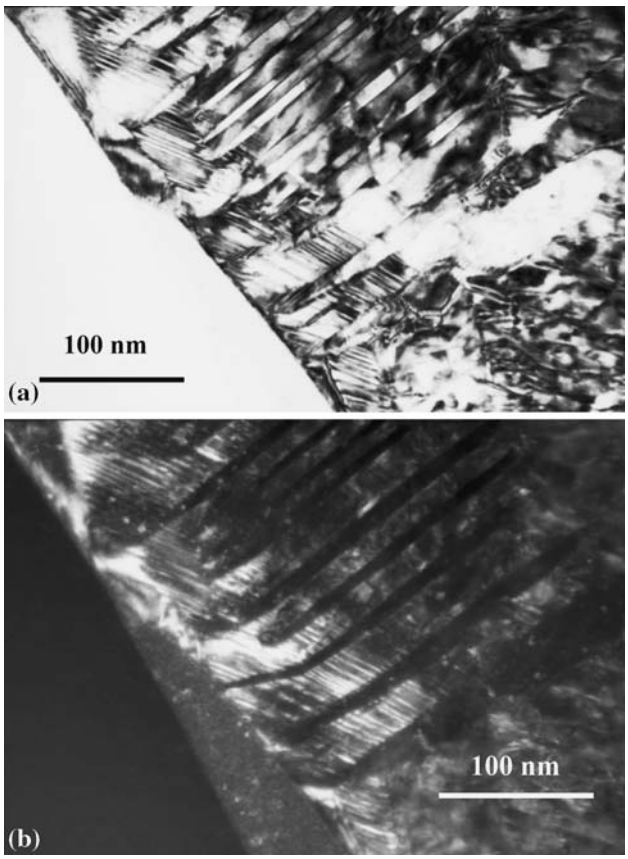

Fig. 12 (**a**) Localized twinning at TiC interface. (**b**) Dark field image

superposition of Figs. 4 and 10. It consisted of three sets of reflections, with one set being common to both the $(11\bar{1})$ Type I twinning pattern and the [011] Type II pattern. The beam direction in the TEM corresponded to $[\bar{1}10]_{M,T1}$ for the $(11\bar{1})$ Type I twins and to $[101]_{T2}//[\bar{1}10]_M$ for the [011] Type II twins, where the subscript M is used to index the set of reflections common to both observed twinning modes. A series of dark field images, formed by placing the aperture around the $(001)_{T1}$, $(00\bar{1})_M$, $(110)_{T1}$, and $(11\bar{2})_M$ reflections, was used to identify the $(11\bar{1})$ Type I twins. The [011] Type II twins were imaged with the $(1\bar{1}\bar{1})_{T2}$ and $(111)_M$ spots. Figure 14b shows the dark field image formed from the $(00\bar{2})_{T1}$ and $(1\bar{1}\bar{1})_{T2}$ reflections.

Region B in Fig. 13 was an area of matrix located adjacent to a TiC_x particle. Selected area diffraction, performed with a beam direction of $[\bar{1}1\bar{1}]_{B2}$, clearly showed reflections at $1/3\{110\}_{B2}$ in the $\langle 110\rangle^*_{B2}$ reciprocal lattice direction. This indicated that the matrix had the R-phase NiTi structure. Dark-field images formed from the $1/3\{110\}_{B2}$ spots did not provide clear pictures of the variant structure.

Region C in Fig. 13 was located in a corridor between two carbide particles. At room temperature the matrix had the R-phase NiTi structure.

Region D was located near the junction of two carbide particles. Figure 15 shows the B19′ morphology both near

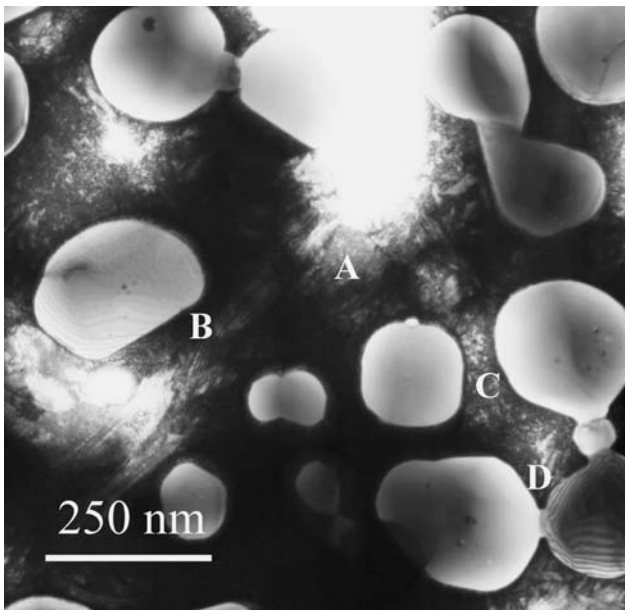

Fig. 13 Global view of area investigated in $TiC_{0.7}$–60NiTi sample

and far from the TiC_x interface. The diffraction pattern for this region (shown in Fig. 16a was composed of at least four sets of reflections. Figure 16b and c shows the indexing. Both [011] Type II twins and $(11\bar{1})$ Type I twins were present. The reflections associated with the [011] Type II twinning mode had the most prominent streaking. These twins were located in the long lamellar variant furthest from the carbide. The variants nearer to the carbide were internally twinned by $(11\bar{1})$ Type I twinning. In most cases the twins extended outward, away from the carbide. Figure 17 shows the variant arrangement near the particle junction.

$TiC_{0.7}$–80NiTi

As-synthesized $TiC_{0.7}$–80NiTI

Room temperature TEM of the matrix of the as-synthesized $TiC_{0.7}$–80NiTi composite only detected the R-phase

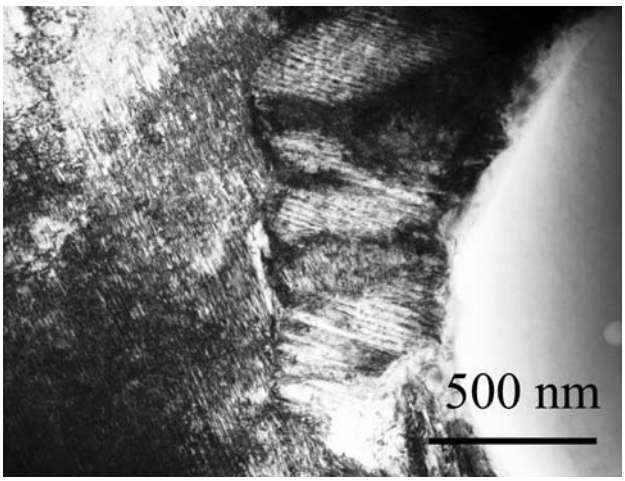

Fig. 15 B19′ morphology near and far from the TiC_x interface of the $TiC_{0.7}$–60NiTi composite in Region D in Fig. 13

structure. Figure 18a shows the morphology. The R-phase variants formed plates, which appeared as alternating dark and light blades. The R-phase variants tended to extend outward, away the carbide particles. Both straight and sawtooth boundaries are present. Figure 18b–d shows a series of dark-field images taken by placing the aperture around the superlattice reflections labeled in Fig. 18a.

Aged $TiC_{0.7}$–80NiTi

The aged $TiC_{0.7}$–80NiTi sample was heated to 350 °C. Since it had a different thermal history than the as-synthesized sample, the microstructures of the samples were compared. As shown in Fig. 19, no differences were visibly evident. The matrix appeared to be composed of plate-like variants that extended outward, away from the carbide. Figure 19 shows the selected area diffraction pattern. Similar to the as-synthesized SAD pattern, the diffraction pattern for the aged samples contains large bright spots with sixfold rotational symmetry and spots at the 1/3 $\{110\}_{B2}$. These features are characteristic of the R-phase

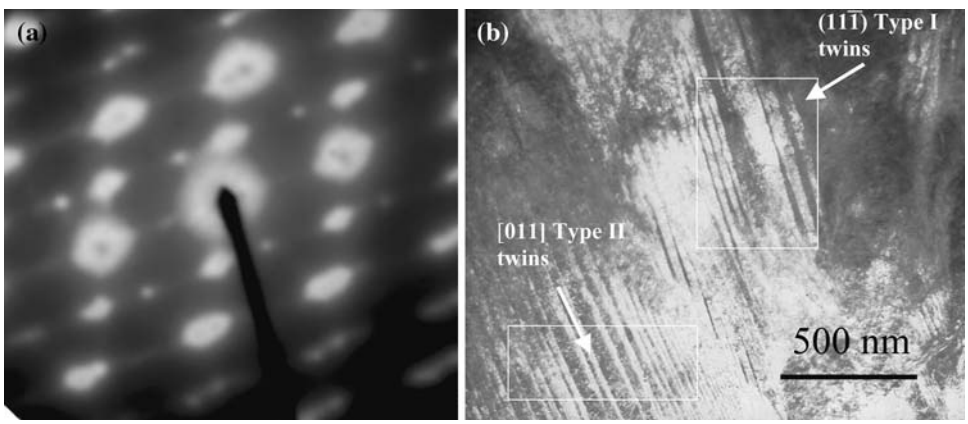

Fig. 14 (**a**) SAD pattern of $(11\bar{1})$ Type I twinning and the [011] Type II twinning. One set of reflections is common to both the $(11\bar{1})$ Type I twinning pattern and the [011] Type II pattern. (**b**) Regions of $(11\bar{1})$ Type I twinning and [011] Type II twinning in the matrix of the 60NiTi composite

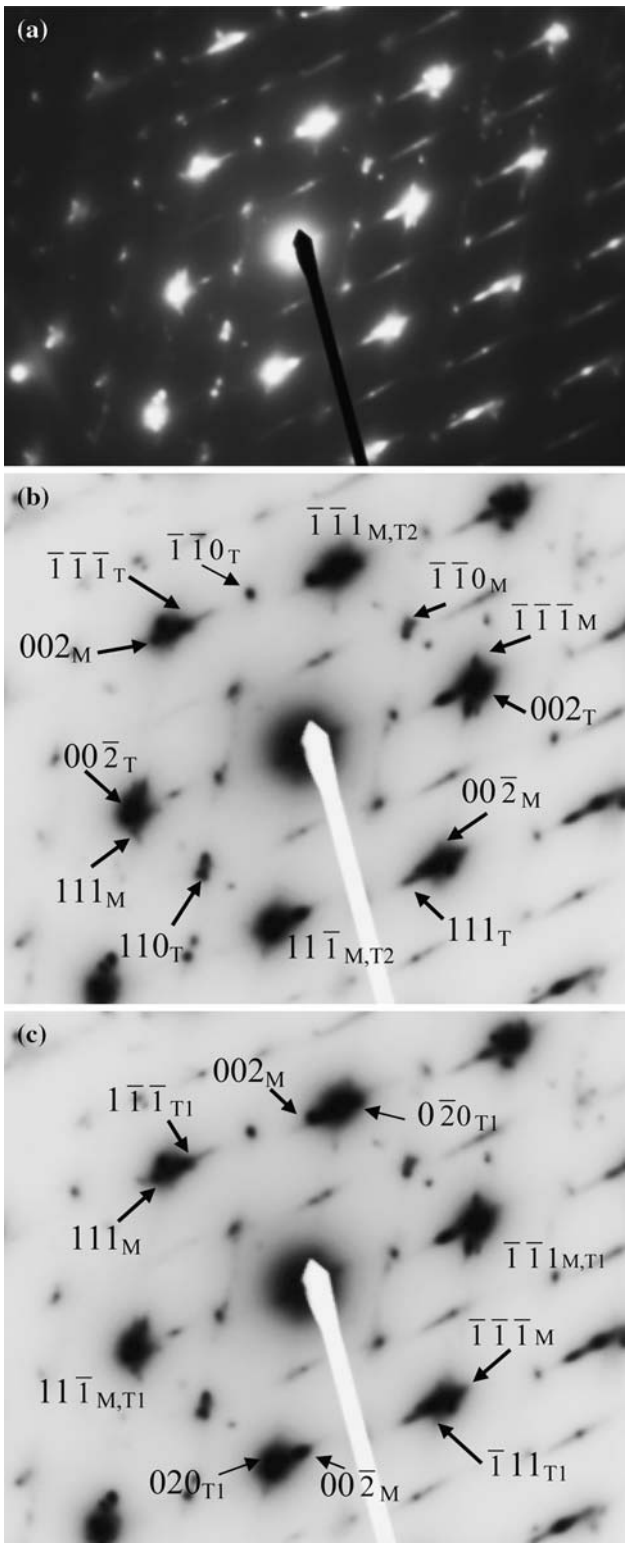

Fig. 16 (**a**) SAD of [011] Type II twins and (11$\bar{1}$) Type I twins near Region D in Fig. 13. (**b**) Indexing of (11$\bar{1}$) Type I twins (**c**) Indexing of [011] Type II twins

structure. However, the SAD taken of the aged $TiC_{0.7}$–80NiTi composite also contains faint spots clustered around the $\{110\}_{B2}$. Comparison of this diffraction pattern with that shown in Fig. 4b of Stroz [21] reveals that these spots are from Ni_4Ti_3 precipitates.

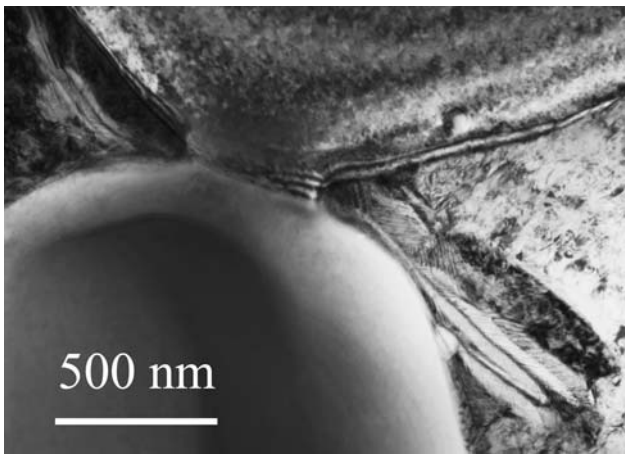

Fig. 17 Variant arrangement near junction of two carbide particles

Differential scanning calorimetry results

Figure 20 shows the calorimetry spectra for the $TiC_{0.7}$–20, 40, 60, and 80NiTi samples during the first and thirtieth thermal cycle. During the first thermal cycle for the $TiC_{0.7}$–20NiTi and $TiC_{0.7}$–40NiTi samples, only one peak appears upon cooling from 150 to −50 °C, even though room temperature TEM showed that the R-phase and B19′ martensite coexist. The absence of multiple peaks on these DSC curves most likely indicates that the R-phase and B19′ transformation temperature ranges overlap. Since there was never any parent B2 phase coexisting with the B19′ martensite in room temperature TEM and the R phase transformation always preceded the B19′ transformation during in-situ TEM (to be phase discussed below) it was assumed that the onset of the peak during cooling marked the R_s temperature. R_s was measured as the temperature where the tangent to the DSC curve at the point of maximum slope intersects the baseline. Table 6 lists the results. Figure 21 compares the R_s temperatures measured in the $TiC_{0.7}$–NiTi composites with measurements made by Miyazaki and coworkers [22] and Gyobu and coworkers [23]. The results are plotted as a function of Ni content, because the transformation temperatures in unreinforced NiTi have been shown to be dependent on composition. Small additions of Ti cause relatively minor variations in R_s (and M_s), while excess Ni significantly depresses the transformations.

The area under the DSC curve is equal to the net enthalpy of transformation Δh_{ch}^{P-M}. For the B2-R transformation, Goo and Sinclair [7] determined that $\Delta h_{ch}^{B2-R} = -3.75$ J/g NiTi

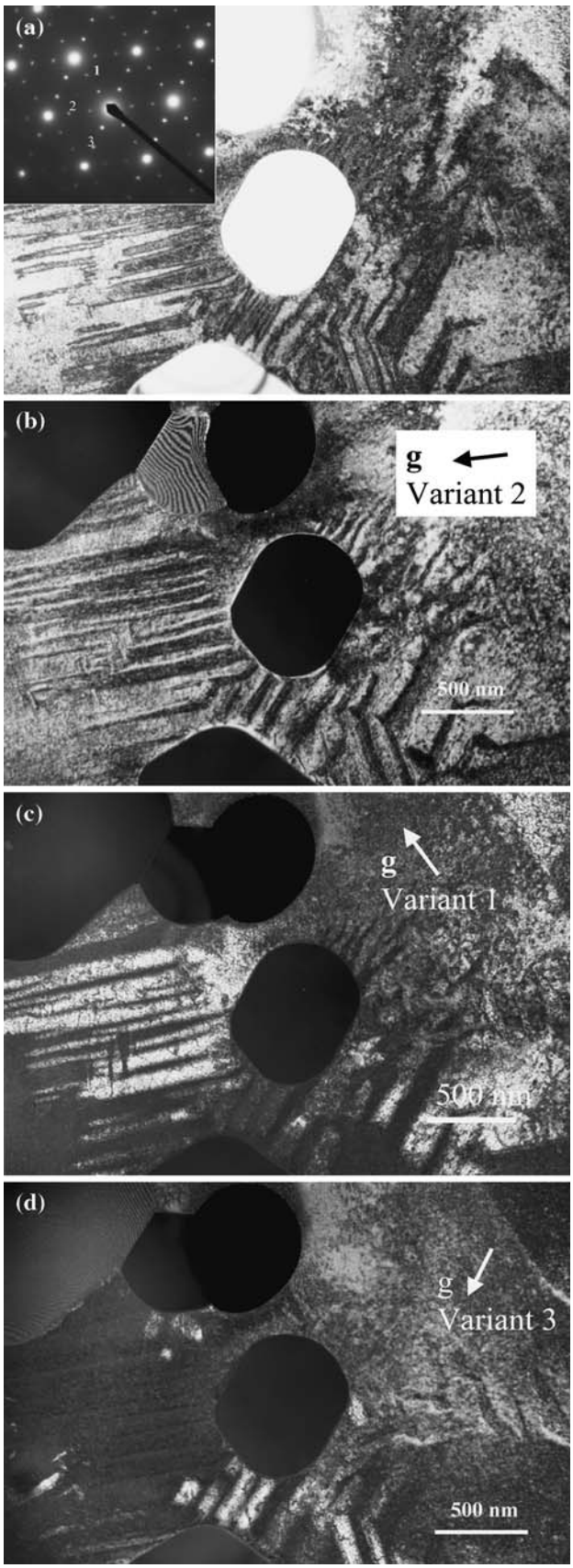

◀**Fig. 18** (**a**) Bright-field image of the matrix of the as-synthesized $TiC_{0.7}$–80NiTi. The R-phase variants formed plates, which appear as alternating dark and light blades. (**b**) Dark field image of Variant 1. (**c**) Dark field of Variant 2. (**d**) Dark field of Variant 3

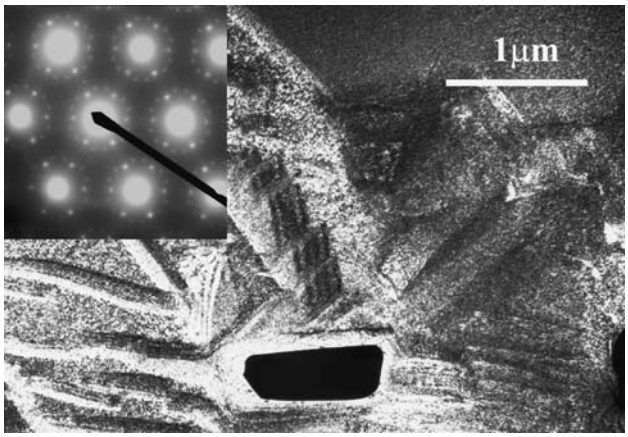

Fig. 19 Dark field image of the matrix of the aged $TiC_{0.7}$–80NiTi sample. Temperature = −150 °C

and for the R-B19′ transformation they determined $\Delta h_{ch}^{R-B19'} = -25.5$ J/g NiTi. The area under the experimental curves during the first thermal cycle for $TiC_{0.7}$–20NiTi and $TiC_{0.7}$–40NiTi was −12.6 J/g NiTi and −25.2 J/g NiTi, respectively. The net enthalpy released during cooling of the composites was always greater than the total energy that would have been released if the entire matrix were to have transformed from B2 to R. The extra energy can only be attributed to the formation of B19′. The M_s was defined so that the area under the curve between R_s and M_s was equal to −3.75 J/g NiTi. It was assumed that the temperature where the peak returns to the baseline defined M_f. Table 6 shows the transformation temperatures. Figure 22 compares the M_s temperatures measured in the $TiC_{0.7}$–NiTi composites with measurements made by Miyazaki and coworkers [22], Honma [24], and Hanlon and coworkers [25]. Mari and Dunand [20] measured a M_s of 70 °C in NiTi, TiC-90NiTi, and TiC–80NiTi composites with a matrix composition of 48.6 at% Ni.

During heating of the $TiC_{0.7}$–20NiTi sample there were multiple peaks. Besides the prominent peak between 83 and 104 °C, there are two smaller peaks, one between 6 and 20 °C, and another starting at 62 °C. During in-situ TEM it was observed during heating that the regions with retained R-phase transformed to B2 first and then B19′ regions transformed directly into B2 without going through the intermediate R-phase. Since the forward and reverse R-phase transformations have a small hysteresis [26] the peak starting at 62° can be attributed to the transformation of any remaining R-phase back to B2. The large peak defines A_s and A_f.

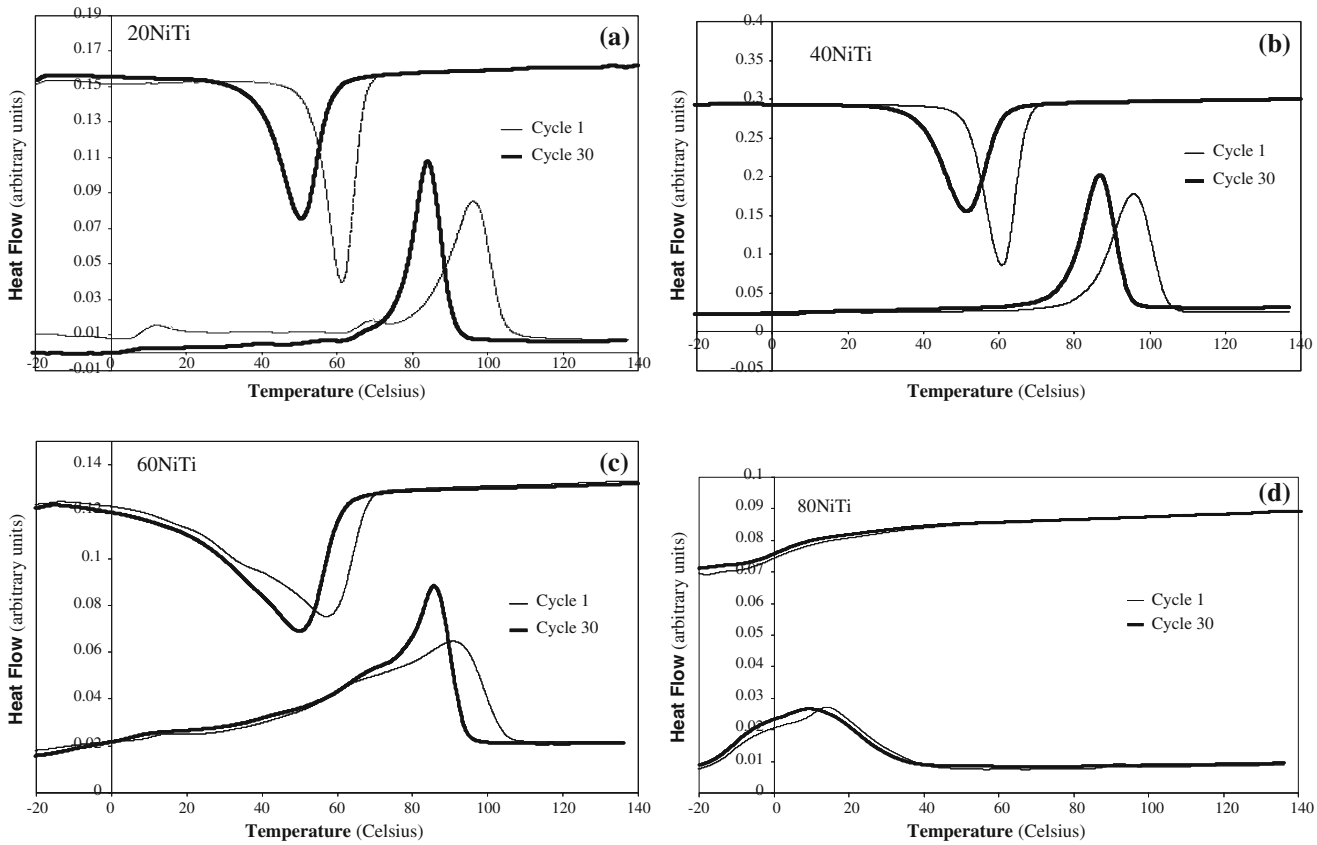

Fig. 20 Calorimetry spectra for (**a**) $TiC_{0.7}$–20NiTi, (**b**) $TiC_{0.7}$–40NiTi, (**c**) $TiC_{0.7}$–60NiTi, and (**d**) $TiC_{0.7}$–80NiTi samples during the 1st and 30th thermal cycle (Scanning rate: 5 °C/min). Curves have been shifted along the vertical axis in order to facilitate comparison of transformation temperatures

Table 6 The transformation temperatures measured in the DSC

	20NiTi	40NiTi	60NiTi	80NiTi	80NiTi (aged)
R_s	67	67	69	16	43
R_f					26
M_s (estimated)	63	64	59		
M_f	52	51	25		

The DSC curves for $TiC_{0.7}$–60NiTi (shown in Fig. 20c) have a more complex shape than the DSC curves for the $TiC_{0.7}$–20NiTi and $TiC_{0.7}$–40NiTi composites. Specifically, several additional peaks appear at temperatures below the main peak and the overall width of the curves is broader. Multiple peaks on the cooling DSC curve may occur if the NiTi matrix undergoes more than one phase transformation (B2–R–B19′). They may also occur when the matrix undergoes a single transformation, if different regions of the material transform over different temperature intervals. The area under the cooling DSC curve was −24.0 J/g NiTi.

Figure 20d shows the DSC curves for the as-synthesized 80NiTi sample. The main peak during cooling begins at a significantly lower temperature than the peaks observed in the other composites. Since the room temperature TEM detected only the presence of the R-phase, there does not appear to be significant overlap of the B2-R and R-B19′ transformation ranges. This suggests that the M_s temperature of the R-B19′ transformation must be below the lowest temperature reached in the DSC. Previous studies by Mari and Dunand [20] have shown that M_s is independent of particle content in TiC–NiTi composites with low volume fractions of reinforcement. In such cases, the M_s only depended on the chemical composition of the alloy. This would suggest that the nickel content in the matrix of the $TiC_{0.7}$–80NiTi composite was greater than 51.0 at% Ni [25].

In the $TiC_{0.7}$–20, 40, and 80NiTi composites the numerical values of R_s are quite close to those reported in thin film NiTi and the numerical values of M_s are quite close to those reported in solution-treated NiTi. In the $TiC_{0.7}$–60NiTi composite, there is a 50 °C shift in R_s and a 130 °C shift in M_s. The chemical content of the matrix was 51.2 ± 0.6 at% Ni, so the expected M_s in unreinforced solution treated NiTi would be between −90 and −40 °C.

Figure 23 shows the DSC curves for the aged $TiC_{0.7}$–80NiTi sample. When compared to the as-synthesized

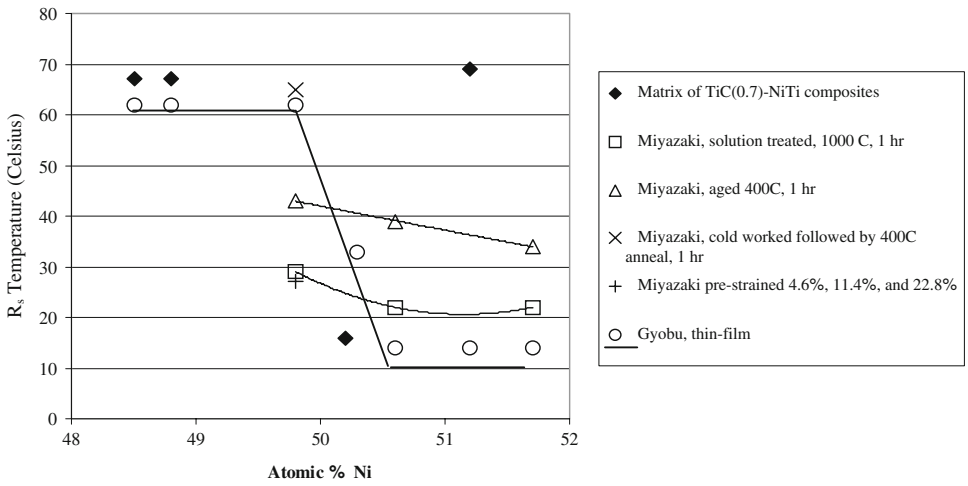

Fig. 21 Comparison of R_s measurements

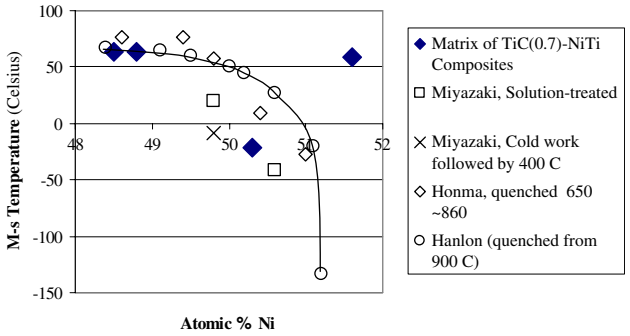

Fig. 22 Comparison of M_s measurements

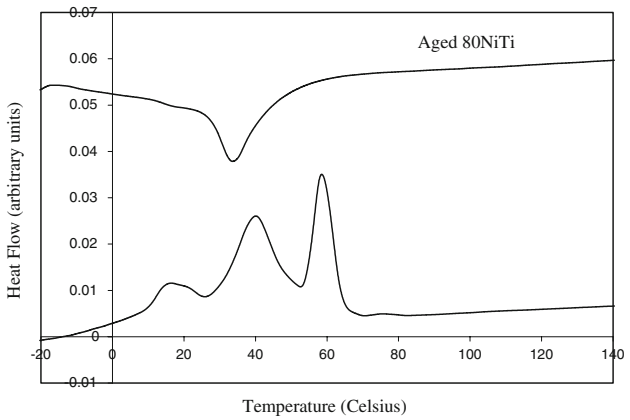

Fig. 23 Calorimetry spectra for aged $TiC_{0.7}$–80NiTi sample. Curves have been shifted along the vertical axis in order to facilitate comparison of transformation temperatures

$TiC_{0.7}$–80NiTi DSC data, it is evident that the forward transformation occurs over a higher temperature interval and the reverse transformation is composed of three separate events. Based on the SAD image shown in Fig. 19, it is apparent that precipitation of Ni_4Ti_3 has occurred in the aged sample. Formation of nickel rich precipitates increases the martensitic transformation temperatures by shifting the nickel content of the matrix toward the stoichiometric composition. It is worth noting that in the aged $TiC_{0.7}$–80NiTi sample the expected increase in the titanium content of the NiTi matrix was not reflected in the EDX measurements reported in Table 5. Although the compositional data were acquired in the spot mode, it was not possible to determine if the probe was focused on the NiTi matrix or on the Ni_4Ti_3 precipitates, because the precipitates were not visible in the image.

Although aging was shown to cause a 27 °C shift in R_s in the aged $TiC_{0.7}$–80NiTi composite, it was not clear if precipitation of Ni_4Ti_3 occurred in the $TiC_{0.7}$–60NiTi composite. The sample was never heated above 180 °C and no evidence of Ni_4Ti_3 was observed. Lenticular precipitates were not seen in the TEM and the characteristic reflections (such as those shown in Fig. 19) were not observed.

Figure 20a–d shows the calorimetry spectra for the $TiC_{0.7}$–NiTi samples after 30 cycles. All the transformation temperatures are lower in the cycled composites. Decrease of M_s and M_f with thermal cycling has also been observed in unreinforced NiTi alloys [20, 22]. In those cases, it was attributed to the introduction and rearrangement of dislocations during the repeated motion of the parent–martensite interface [22]. Figure 24 shows dislocations introduced by thermal cycling in the $TiC_{0.7}$–40NiTi composite.

TEM of the thermally cycled $TiC_{0.7}$–40NiTi composite showed that cycling also resulted in a change of transformation path. As shown in Fig. 25, after 30 cycles, B2 and B19′ martensite were observed to coexist in the matrix of the 40NiTi sample. The B2–B19′ transformation occurred without the appearance of the R-phase. This is different from the behavior observed in unreinforced, solution treated NiTi where thermal cycling tends to favor the B2 → R → B19′ transformation. Miyazaki and coworkers [22] explained the enhancement of the R-phase upon cycling unreinforeced NiTi by noticing that R_s remains constant with increasing number of cycles, while M_s

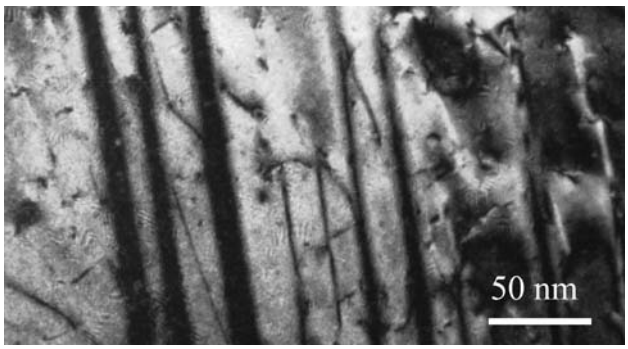

Fig. 24 Dislocations in matrix of thermally cycled $TiC_{0.7}$–40NiTi

decreases. This leads to a broadening of the R-phase stability range. In the $TiC_{0.7}$–40NiTi composite, reduction of M_s with thermal cycling was observed, but the R-phase was inhibited. Mari and Dunand [20] also observed suppression of the R-phase in TiC-90NiTi and TiC–80NiTi after 100 thermal cycles.

Figure 26 shows the microstructure of the matrix of the thermally cycled $TiC_{0.7}$–40NiTi sample. It shows banded features similar to those in Fig. 1a of Madangopal and Singh [18]. Madangopal and Singh [18] argued that the banded features correspond to "ghost structures" from internal [011] Type II twins. They suggested that transformation cycling causes the accumulation and arrangement of defect structures, which become imprinted in the parent B2 phase.

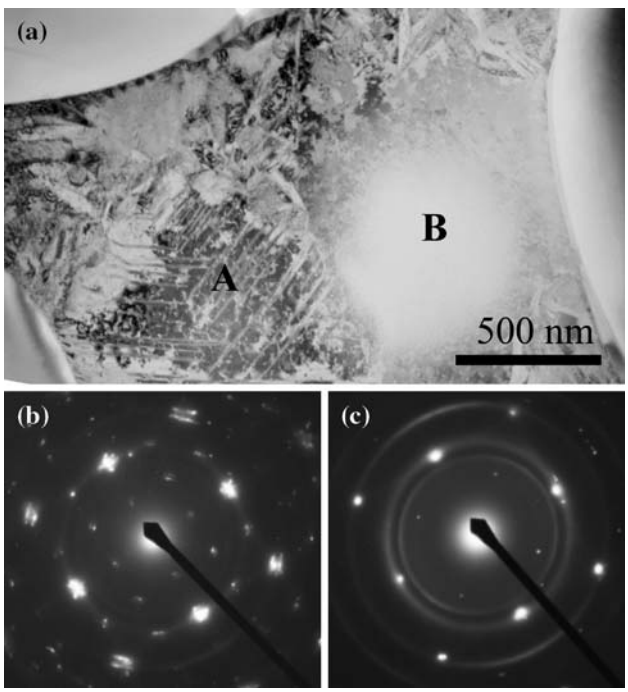

Fig. 25 (**a**) Structure of matrix of $TiC_{0.7}$–40NiTi sample after 30 cycles. (**b**) SAD of Region A with multivariant B19′. (**c**) SAD of Region B with parent B2 structure. Zone axis $[001]_{B2}$

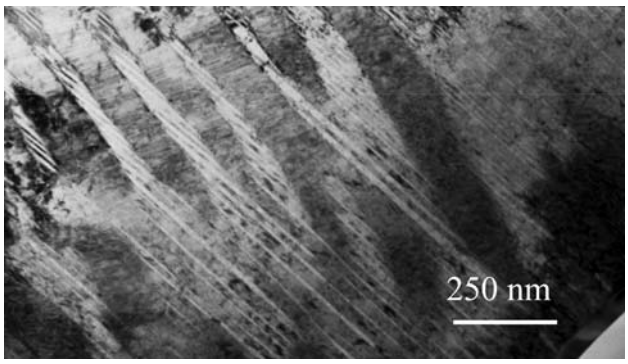

Fig. 26 Matrix of thermally cycled $TiC_{0.7}$–40NiTi. Banded regions are similar to those reported by Mandangopal and Singh [18] and may be the vestiges of prior martensite twins

In-situ TEM

In-situ heating and cooling was used to investigate the transformation path, martensite nucleation and growth, and the effect of carbide particles on the movement of NiTi transformation fronts. The samples were first heated to 110 °C (above the A_f temperature). This process was performed in stages to record selected area diffraction patterns, bright field images, and dark field images at specific temperatures. The experiments were also recorded on video. Then the samples were cooled in stages to room temperature in order to observe the martensitic forward temperature. Again selected area diffraction patterns, bright field images, and dark field images at specific temperatures were recorded. In most cases the R → B19 transformation was incomplete at room temperature, so liquid nitrogen was added to cool the specimen even further.

$TiC_{0.7}$–20NiTi

On heating the thin foil, the regions with retained R-phase were the first to transform (Region A of Fig. 2). The R–B2 transformation started at 56 °C. When the SAD pattern was observed at 60 °C, the intensity of the R-phase spots (located at the $1/3\{110\}_{B2}$ positions) was diminished. At 70 °C, the R-phase reflections were no longer visible. At 71 °C, the B19′ variants located at the B2–B19′ interface (formerly the R–B19′ interface) began to transform. They reverted directly to the parent B2 phase without passing through the intermediate R-phase.

During cooling, the B2 → R transformation occurred first. The nucleation and growth of the R-phase transformation was not directly imaged in the TEM. This transformation was only identified by the presence of spots at the $1/3\{110\}_{B2}$ positions in the SAD. The R-phase reflections were first noticed at 40 °C and appeared strongest in regions that were adjacent to carbide particles. By 29 °C the entire matrix had the R-phase structure.

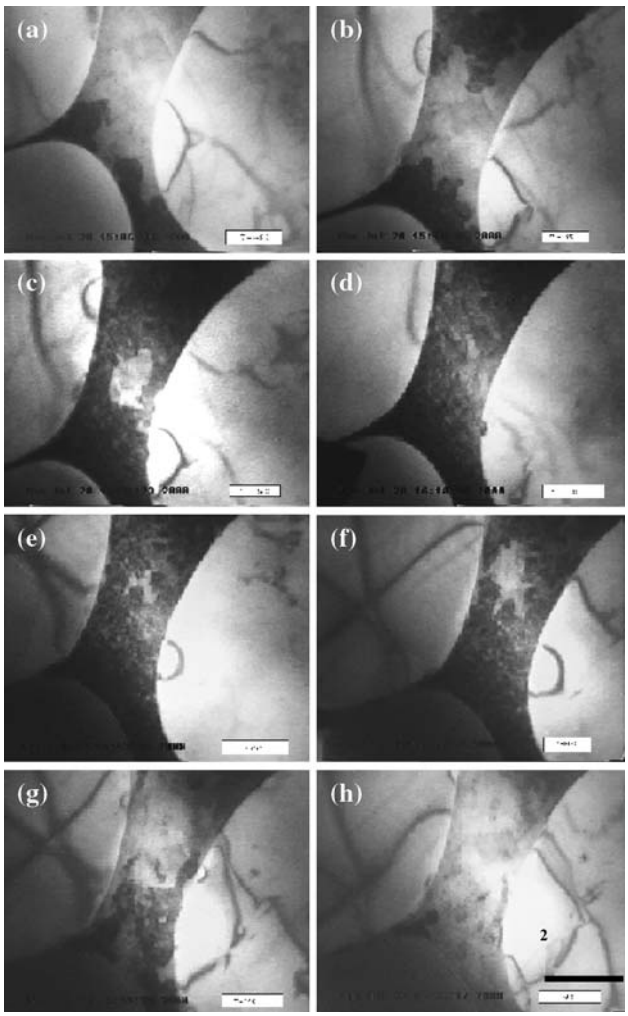

Fig. 27 In-situ experiments in 20NiTi. Top four pictures depict the R → B19 transformation upon cooling. Lower four pictures depict the B19′ → B2 transformation upon heating. Starting in top left and continuing across and then down the temperatures are as follows: (**a**) $T = -45$ °C; (**b**) $T = -65$ °C; (**c**) $T = -86$ °C; (**d**) $T = -112$ °C; (**e**) $T = 74$ °C, (**f**) $T = 80$ °C; (**g**) $T = 85$ °C; and (**h**) $T = 86$ °C

With further cooling, the R → B19 transformation began. Fortunately, it was possible to record this transformation. The sequence is shown in Fig. 27a–d. The specimen was tilted so that the R-phase appeared with light contrast and the B19′ appeared with dark contrast. The first B19′ variants were detected at −12 °C. As shown in Fig. 28, the B19′ nucleated at the intersection of a grain boundary in NiTi with the $TiC_{0.7}$ particle. In this region, the activation energy for transformation is lower. As the temperature was lowered, it grew in bursts, separated by as much as 30 °C intervals. The transformation front moved along the carbide particle interfaces and the NiTi grain boundaries before spreading throughout the matrix. In Fig. 27c the remaining R-phase appeared as an island surrounded by B19′. At −112 °C only the smallest amount of R-phase remained.

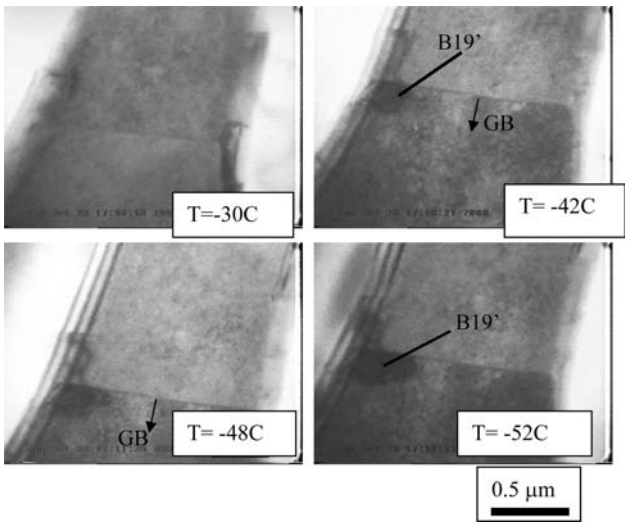

Fig. 28 Nucleation of B19′ at the intersection of a $TiC_{0.7}$ interface and a NiTi grain boundary in $TiC_{0.7}$–20NiTi

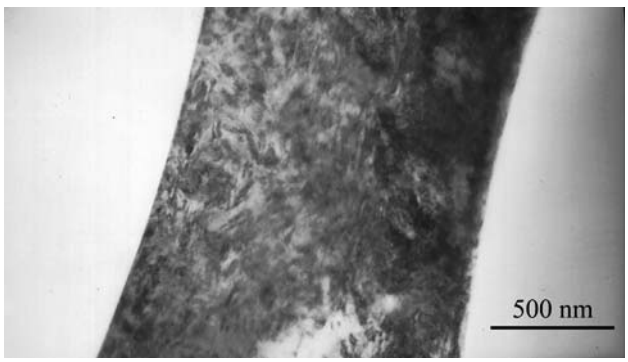

Fig. 29 B19′ martensite formed in thin foil ($TiC_{0.7}$–20NiTi). Same area as in Fig. 3b

Figure 29 shows the same area of the matrix as in Fig.3b. The large variant with [011] Type II twinning that was located on the left-side in Fig. 3b has been replaced by many smaller variants. This change in variant structure was not surprising, because the morphology in Fig. 3b was formed in the bulk condition, while the variant arrangement in Fig. 29 was formed by heating the thin foil above A_f and then cooling it below M_f. The stress conditions in the two cases were not the same. The B19′ that formed in the bulk condition was subject to tridimensional constraint, while the B19′ that formed in the foil was subject to stress relaxation at the foil surfaces.

Upon heating, for a second time, the retained R-phase regions of the matrix were the first ones to transform to the B2 phase. Then, as the temperature was increased, the last B19′ martensite plates that formed during cooling were the first to revert back to the parent B2 structure. The B19′ regions transformed directly to the B2 phase, without passing through the R-phase.

$TiC_{0.7}$–40NiTi

The in-situ transformation of the matrix of the 40NiTi sample followed the same course as it did in the 20NiTi, except the numerical values of the transformation temperatures were higher. Again, the formation of the R-phase was only apparent from the SAD. No distinct morphology was observed. The R-phase reflections first appeared at 42 °C .

The beginning of the B19′ transformation started at 34 °C, when a dark patch appeared in the narrow corridor in the upper right-hand corner of the image. No further growth or new nucleation was observed until the temperature was reduced to 11 °C. At that point, the transformation was characterized by the sudden appearance of several dark branches emanating from the same corridor that had previously transformed at 34 °C. The B19′ looked as if it were a river spilling onto a flood plain. One branch extended completely across the broad region of matrix to the narrow corridor in the lower left-hand corner of the image. The next series of transformation bursts occurred when the temperature dropped below 4 °C. The long branches began to widen in a series of small jumps and the matrix in the upper left-hand corner transformed. The transformation appeared to be complete at −13 °C. However, when other regions of the foil were imaged and SAD patterns were recorded, it became evident that the R-phase still existed in the thinnest areas.

Figure 30 shows images taken at three temperatures: room temperature, above A_f, and below M_f. The wavy martensite in the upper left-hand corner of the image maintained the B19′ structure even when the sample was heated to 110 °C.

$TiC_{0.7}$–60NiTi

Region A (in Fig. 13)

In-situ heating of the foil was performed in a series of steps, so that the progression of the reverse transformation could be studied. In Region A of Fig. 13 there was no noticeable change in the SAD pattern at 50 °C. At 70 °C, the dark-field image from the $(00\bar{2})_{T1}$ and $(1\bar{1}\bar{1})_{T2}$ showed that matrix was partially transformed to B2. At 108 °C, only a small amount of B19′ remained near a carbide particle.

To observe the propagation of martensite during cooling, the microscope was originally focused on the retained B19′. Dark-field imaging was used, so that any further extension of the B19′ would show up as light contrast against a black background. No change was observed from 108 to 22 °C.

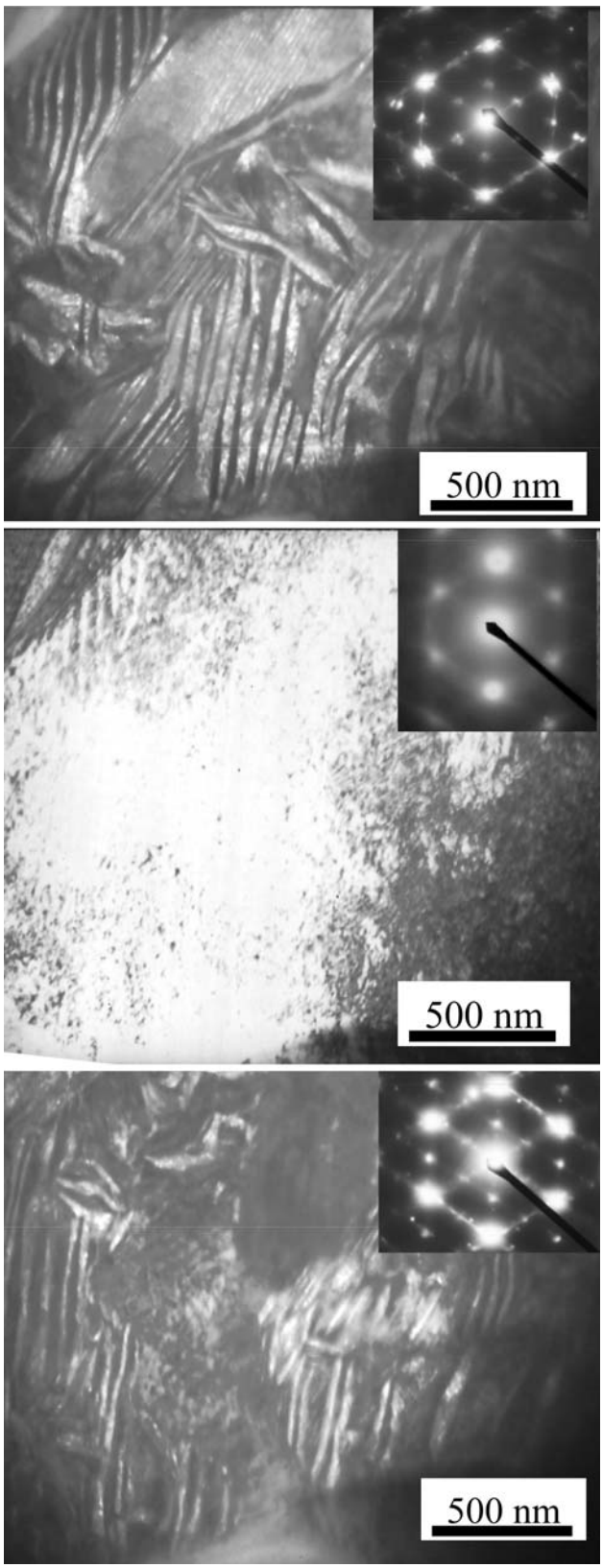

Fig. 30 $TiC_{0.7}$–40NiTi imaged in in-situ heating experiment; *Top*: $T = 22$ °C. B19′ martensite formed in bulk condition; *Middle*: $T = 110$ °C. B2 NiTi; *Bottom*: $T = 27$ °C. B19′ formed in thin foil

Nearby, at 22 °C, SAD showed that the R-phase transformation had occurred, but dark-field images formed from the reflections located at the $1/3\{110\}_{B2}$ positions did not show a distinct variant structure. Liquid nitrogen was added to drop the temperature below room temperature. By −100 °C, the B19′ transformation had begun and the front was moving away from the carbide particles and toward the hole. This B19′ variant structure, formed in the thin foil, was very different from that formed in the bulk condition. Instead of the lamellar morphology shown in Fig. 14, the B19′ variants formed in the foil were smaller and lens shaped.

Region B (in Fig. 13)

After heating the TEM foil to 50 °C, selected area diffraction was performed on Region B of Fig. 13. The multivariant R-phase structure that was present at room temperature had mostly transformed to B2. Only the reflections from one R-phase variant could be detected, and the intensity was very low. The transformation to B2 was complete by 70 °C. During cooling from 108 °C, no change was detected until 22 °C. Diffraction patterns at this temperature showed that the R-phase had reappeared, even though the R-phase transformation front had not been noticed. At −22 °C, the B19′ martensite still had not nucleated. By −104 °C, the B19′ martensite had nucleated at the carbide interface and was growing outward, away from the particle. Figure 31 shows a dark field image of the B19′. The B19′ martensite variants were lens shaped and approximately 250 nm long and 50 nm wide. Images showed that islands of R-phase NiTi still existed in the broad corridors. SAD confirmed the coexistence of B19′ and R-phase NiTi.

Region C (in Fig. 13)

During in-situ heating, Region C of Fig. 13 had almost completely transformed from R-phase NiTi to the parent B2 structure by 50 °C. This change was only detected by SAD. The reverse transformation was not apparent in the TEM image. When the foil was cooled back to room temperature, the matrix in the corridor between the carbide particles returned to the R-phase. At −50 °C, no B19′ was detected. After cooling to −104 °C, multivariant B19′ appeared on the diffraction pattern.

$TiC_{0.7}$–80NiTi

Unlike the other composites, at room temperature the matrix of the 80NiTi composite only consisted of the R-phase structure, whose morphology could be clearly

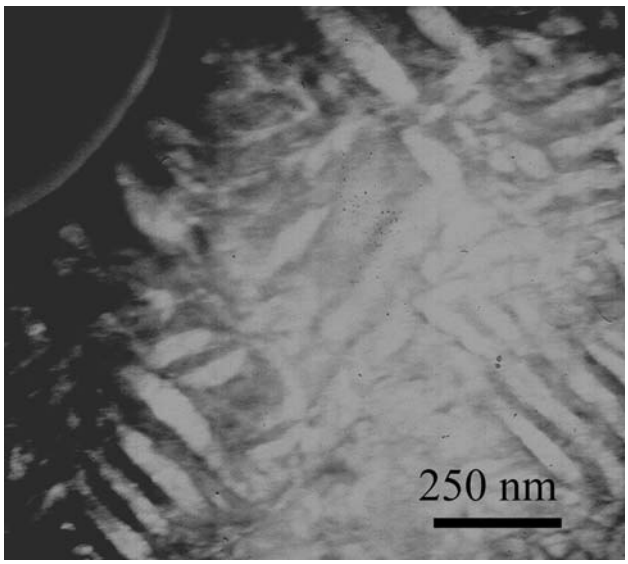

Fig. 31 Lens shaped B19′ martensite formed after heating the TEM foil to 108 °C and then cooling to −104 °C in $TiC_{0.7}$–60NiTi

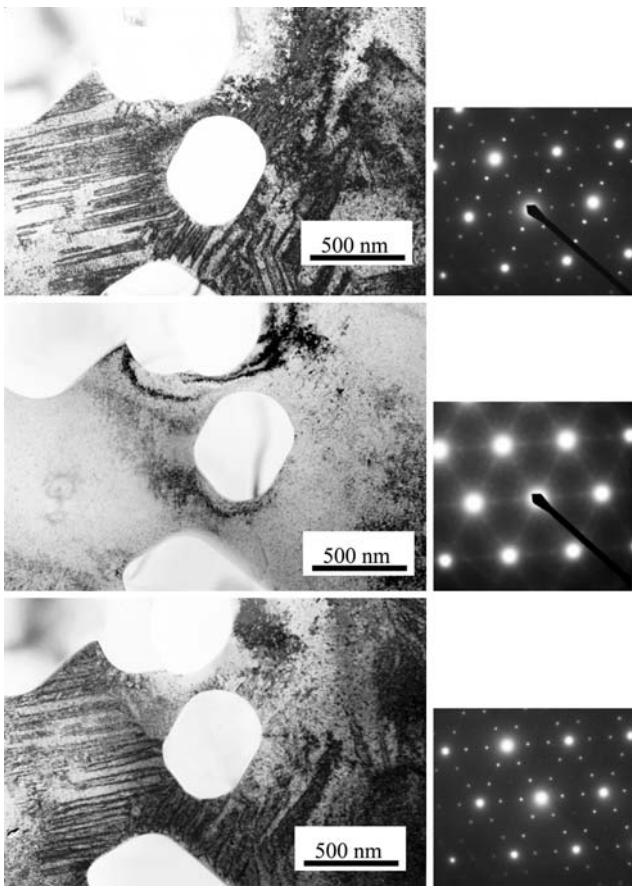

Fig. 32 *Top*: Matrix of 80NiTi at room temperature. Matrix has R-phase structure. Variant structure formed in bulk condition. *Middle*: $T = 108$ °C Matrix has B2 structure. *Bottom*: $T = -3$ °C Matrix has R-phase structure. Variant arrangement same as in top picture, but formed in thin-foil

imaged. As shown in the top photo of Fig. 32, the R-phase variants formed plates that extended away from the central carbide particle. The accompanying SAD pattern shows that no B19′ reflections were evident.

After heating to 110 °C the R-phase reverted to the parent B2 structure. The region shown in the middle photo of Fig. 32 consisted of a single NiTi grain. As with all the composites, the NiTi grain size was much larger than the $TiC_{0.7}$ particle size.

During cooling, the B2 → R transformation started at 15 °C. By −3 °C most of the thicker areas of the matrix had the R-phase structure. Surprisingly, the variant arrangement after the in-situ transformation appeared to be the same as that formed in the bulk condition. There was no apparent thin foil effect, as had been observed in the other composites during the R → B19′ transformation. In an attempt to observe the R → B19′ transformation in the 80NiTi sample, the temperature in the TEM was reduced to −138 °C. No B19′ reflections appeared.

Conclusions

Electron microscopy showed the details of transformation sequence, phases, and interfaces in $TiC_{0.7}$–NiTi composites made by combustion synthesis followed by quasi-isostatic pressing (QIP). The following conclusions can be made:

1. The interface between the $TiC_{0.7}$ spheroidal phase and the continuous NiTi phase is exceptionally clean. This is consistent with the fracture pattern observed in the specimens subjected to mechanical testing: cracks propagated preferentially through the $TiC_{0.7}$ particles and not along interface with NiTi.
2. At room temperature, the matrix of the as-synthesized 20NiTi, 40NiTi, and 60NiTi composites contains both R and B19′ martensite. No distinct R-phase morphology could be imaged.
3. In the B19′ martensite, [011] Type II twinning, $(11\bar{1})$Type I twinning and (001) compound twinning modes were observed as the LIS of the R-B19′ transformation. The [011] Type II twinning is often reported as the LIS of the B2-B19′ transformation, but this is the first experimental confirmation of its predicted presence as a qualified LIS of the R-B19′ transformation. The (001) compound twinning mode was the fine structure of the martensite with a wavy morphology. Twinning was also observed at the interface with carbide particles, which confirms that some stress relaxation of the elastic mismatch occurs.
4. At room temperature, the matrix of the 80NiTi composite had the R-phase structure, which appeared with a needle-like morphology.
5. Thermal cycling resulted in the suppression of the R-phase transformation in the $TiC_{0.7}$–40NiTi composite. This is the opposite of the behavior observed in unreinforced NiTi alloys.

Acknowledgement This research was supported by the Director, Office of Science, Office of Basic Energy Sciences of the US Department of Energy under contract No. DE-AC03-76SF00098.

References

1. Merzhanov AG, Borovinskaya IP (1972) Dokl Akad Nauk SSSR 204:336
2. Gordopolov Y, Merzhanov A (1993) AIAA 154:539
3. Shikhverdiev RM, Yu A (1992) Intl J SHS 1:64
4. Munir ZA, Anselmi-Tamburini U (1989) Mater Sci Rep 3:277
5. Yi HC, Moore JJ (1990) Mater Sci 25:1159
6. Strutt ER, Olevsky EA, Meyers MA (2008) Paper 1: Combustion synthesis/quasi-isostatic pressing of TiC–NiTi cermets: processing and shrinkage anisotropy (in press)
7. Goo E, Sinclair R (1985) Acta Metall 33:1717
8. Hara T, Ohba T, Okunishi E, Otsuka K (1997) Mater Trans JIM 38:11
9. Hehemann RF, Sandrock GD (1971) Scripta Metall 5:801
10. Otsuka K, Sawamura T, Shimizu K (1971) Phys Status Solida A 5:457
11. Jacobs K, Sehitoglu H, Balszer M (1996) Metall Mater Trans A 27A:3066
12. Miyazaki S, Otsuka K, Wayman CM (1989) Acta Metall 37:1837
13. Hwang CM, Meichle M, Salamon MB, Wayman CM (1983) Philos Mag A 47:9
14. Knowles KM, Smith DA (1981) Acta Metall 29:101
15. Onda T, Bando Y, Ohba T, Otsuka K (1992) Mater Trans JIM 33:354
16. Nishida M, Ohgi H, Itai I, Chiba A, Yamauchi K (1995) Acta Metall Mater 43:1219
17. Xie Z, Liu Y, Van Humbeeck J (1998) Acta Mater 46:1989
18. Madangopal K, Singh JB (2000) Acta Mater 48:1325
19. Zijlstra SR, Beijer J, Klostermann JA (1974) J Mater Sci 9:145
20. Mari D, Dunand DC (1995) Metall Mater Trans A 26A:2833
21. Stroz D (1997) J Phys IV C5:C5–293
22. Miyazaki S, Igo Y, Otsuka K (1986) Acta Metall 34(10):2045
23. Gyobu A, Kawamura Y, Harikawa H, Saburi T (1996) Mater Trans JIM 37:697
24. Honma T (1987) In: Funakubo H (ed) Shape memory alloys. Gordon and Breach, New York, NY
25. Hanlon JE, Butler SR, Wasilewski RJ (1967) Trans Met Soc AIME 239:1323
26. Todoroki T (1990) In: Duerig TW (ed) Engineering aspects of shape memory alloys, Butterworth and Co., London, p 315